Nanoscale

PAPER

View Article Online
View Journal | View Issue

Cite this: *Nanoscale*, 2015, **7**, 13537

Structural characterisation of printable noble metal/poly(vinyl-alcohol) nanocomposites for optical applications

A. C. Hourd,[a,b] R. T. Baker[b] and A. Abdolvand*[a]

Received 2nd June 2015,
Accepted 10th July 2015

DOI: 10.1039/c5nr03636d

www.rsc.org/nanoscale

In order to enable exploitation of noble metal/poly(vinyl-alcohol) nanocomposites for device fabrication, solutions of poly(vinyl-alcohol) suitable for piezo-driven inkjet printing techniques are identified and discussed in terms of their material properties. The printable poly(vinyl-alcohol) medium is then exploited as a host material through the formation of silver or gold nanoparticles in order to create nanocomposites that exhibit a surface plasmon resonance behaviour associated with the small metallic inclusions. To mitigate some of the material redistribution effects associated with the drying of printed droplets containing finely divided materials, the metallic nanoparticles are formed *after* the printing and drying process is completed, by way of an *in situ* reduction of an appropriate metal salt by the poly(vinyl-alcohol)-host matrix itself, which takes place at modest temperatures compatible with most substrate materials. An obvious application for such nanocomposites is in optical elements whereby the surface plasmon resonance associated with the metal is the functional aspect of devices such as sensors or active optical elements. High Resolution Transmission Electron Microscopy was used to examine the dimensions, distribution, morphology and crystal structure of the silver and gold nanoparticles in detail allowing discussion of their suitability for these applications and what further optimisation may be necessary to adequately control their formation.

1. Introduction

Deposition of materials using industrially scalable inkjet printing technology is already establishing itself as a viable method for manufacturing a wide range of functional devices.[1–5] Such printing technologies frequently require the functional material in nanoparticle form in order to create a colloidal dispersion to act as the "ink", whereby the formulation of the printable fluid not only has to have a rheology compatible with the process of droplet formation but also needs to control the distribution of the nanoparticulate material upon coalescence and drying of the deposited droplets. This latter problem, the so-called "coffee-stain" effect, is well known[6–12] and can be particularly troublesome for the case of small nanoparticles being exploited for their unique optical properties.[13] Uniformly printed distributions of the nanoparticles are usually achieved by the careful selection of multi-component solvent delivery systems,[14,15] which may be time-consuming to optimise and prepare.

Here we demonstrate a straightforward method of inkjet printing silver or gold nanoparticles contained within a host matrix of poly(vinyl-alcohol) (PVA) that considerably reduces the problem of nanoparticle redistribution by "coffee-stain" type effects. This is achieved by holding the metal in solution form within the PVA precursor throughout the inkjet droplet delivery process and subsequent coalescence and drying (gelling) of the printed pattern. We then exploit the somewhat unique and well documented properties of the chemical environment within the PVA host medium[16–22] to form, *in situ*, the Ag or Au metal nanoparticles within the printed polymer using a modest ambient thermal treatment compatible with a wide range of substrate materials, including the flexible plastics typically used in roll-to-roll manufacturing. This opens up a route for readily fabricating devices from these nanocomposite materials on either supported or free-standing platforms.

In order to assess the uniformity of the printable nanocomposite materials prepared by this route, a detailed study of the structure of the synthesised nanoparticles is presented. The growth characteristics of the nanoparticles and what further optimisation may be necessary to control their formation so as

[a]*School of Engineering, Physics and Mathematics, University of Dundee, Dundee DD1 4HN, UK. E-mail: a.abdolvand@dundee.ac.uk*
[b]*School of Chemistry, University of St Andrews, St Andrews, Fife KY16 9ST, UK*

to produce viable platforms for surface plasmon resonance (SPR) based optical devices are discussed.

2. Experimental methods

Printing of the PVA-based materials was carried out using a FujiFilm Dimatix DMP-2831 materials printer equipped with cartridges producing 10 pl volume droplets by way of piezo-driven actuators. The platen of this printing system could be heated to optimise drying conditions of the printed droplets and the print cartridge can also be heated to tune the viscosity of the jettable fluid. Images of droplet formation were captured using the printer's "Drop Watcher" in-built imaging system.

For study by High Resolution Transmission Electron Microscopy (HRTEM), samples were prepared by forming free-standing PVA nanocomposite films by spin-coating (at 5000 RPM) the polymer material onto a glass slide pre-coated with a release layer. This resulted in the very thin (~100 nm) PVA-nanocomposite films required for TEM analysis, portions of which could then be floated from the substrate by immersion in an appropriate solvent to dissolve only the release layer and captured directly onto standard 3 mm Cu TEM grids (without holey carbon) for examination in the microscope. The instrument used was a JEOL JEM 2011 (a modified 2010 unit) TEM operating at 200 keV with a LaB_6 filament and having a structural resolution of 0.194 nm. The instrument was equipped with a Gatan CCD camera operated using Digital Micrograph 3.34 software. This software was also used to calculate Fast Fourier Transforms (FFTs) from selected regions of the digital images to give Digital Diffraction Patterns (DDPs) and for the analysis of these. In some cases, reverse FFTs were performed on selected spots in the DDPs in order to regenerate partial images and so relate specific diffraction spots to features in the original image. DDPs can be analysed in a similar way to true diffraction patterns recorded in the TEM instrument but are more convenient when considering very small areas of the sample, as in this contribution.

Image analysis of the lower magnification TEM images to determine particle size distribution was carried out in the freely available software package *ImageJ*.[23,24]

Light microscope images were captured using a KEYENCE VHX-1000 Digital Microscope system and the thickness of the lines was assessed using a Dektak 3-ST surface profiler. Surface tension measurements were carried out *via* drop shape modeling using a Krüss EasyDrop system, whilst viscosity was measured using a Cannon–Fenske viscometer tube immersed in a constant temperature bath. Optical characterization of the samples (on glass substrates) was performed using a JASCO V-670 UV/VIS/NIR spectrophotometer.

3. Results and discussion

3.1 Jettable form of PVA host material

A particular driver behind this work was to enhance the potential for printed optical device components to complement the current extensive field of printable electronics. PVA offers a host polymer matrix having excellent optical properties[25] and is very amenable to accommodating other optically active materials in order to exploit their behaviour.[26,27] However, PVA solutions can be far from ideal rheologically as printable media (PVA is usually added to printable fluids only in small quantities for viscosity adjustment or to act as a binder) and careful consideration needs to be given to the properties of the stock PVA material used to make the precursors jettable.

For piezo-driven inkjet printing, the commercially available printing systems usually specify a restricted range of fluid properties such as viscosity, surface tension, volatility and maximum size of contained particulate. For PVA solutions, viscosity at a given temperature and concentration is highly dependent upon the molecular weight of the solid starting material, decreasing in proportion to the degree of polymerisation.[28] The degree of hydrolysation of the poly(vinyl-acetate) used to manufacture the PVA has only a very small influence on the viscosity but greatly affects the surface tension of the resulting water-based solutions of PVA,[28,29] as conversion from the acetate to the alcohol form amounts to a saponification process,[30] essentially giving inherent surfactant properties to the resulting solution for lower degrees of hydrolysis. As the viscosity of the printable fluid can be tuned over a moderate range by heating the printing cartridge, surface tension control then becomes the critical parameter to optimise by strategic choice of the PVA's degrees of hydrolysis, polymerisation and concentration (it should be noted that adding further surfactant to a PVA solution was found not to be an effective way of adjusting the surface tension).

From a designed set of experiments, our surface tension measurements indicated that a 4 wt% solution in de-ionised water of PVA having an 87–89% degree of hydrolysation and degree of polymerisation in the range 295–520 monomer units had a surface tension of 52.0 ± 0.5 mN m^{-1}, which is at the upper limit but still within the manageable range for printability. The 4 wt% PVA solution also had a room-temperature (23 °C) viscosity of 3.28 ± 0.05 cP, again within the limits for printability, and was therefore selected as the base formulation of the printable host medium. As seen from Fig. 1, which shows the PVA solution leaving the nozzles of the cartridge print-head, well-formed droplets could be generated with a 10 pl print cartridge by using an appropriately designed piezo-driver waveform to cope with any non-Newtonian (shear thinning) behaviour of the PVA solution. This resulted in perfectly spherical droplets (Fig. 1(b)) that would form well before impacting the substrate, which was situated 1 mm below the print-head.

3.2 Nanocomposite printing

Having identified a printable PVA host matrix, a noble metal complex precursor could then be added to the PVA solution to enable growth of the nanoparticles and form the composite materials. In our work, the precursor was either silver nitrate, which was added to the PVA solution to yield an ultimate concentration of approximately 15 mM in the final printable fluid

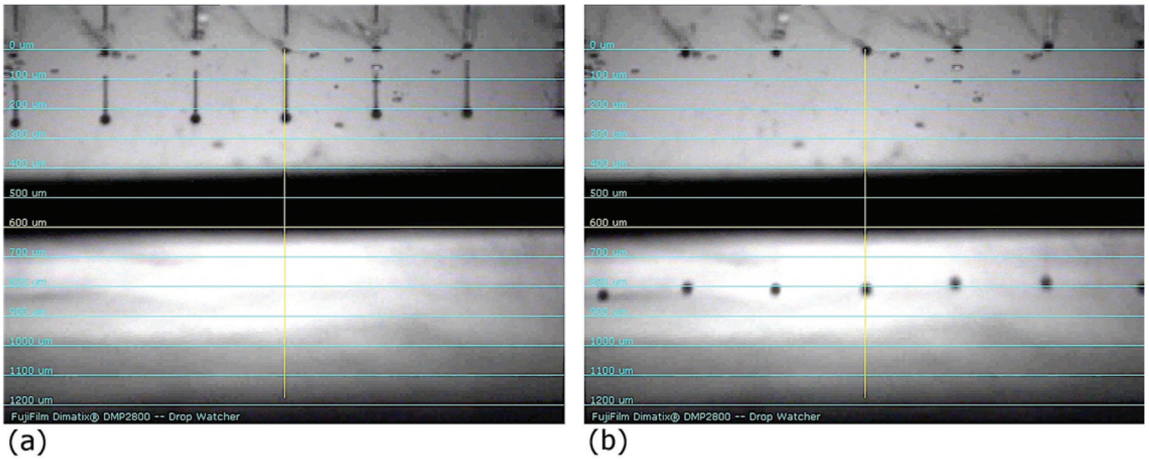

Fig. 1 Droplet formation for printable PVA nanocomposite fluid. (a) Immediately after ejection from printer nozzles showing the short droplet "tails" with no satellite droplet structure for the optimised driver waveform. (b) Formation of well-behaved droplets after absorption of the "tail" into the main droplet body, well before impact with the substrate.

or hydrogen tetrachloroaurate(III) with a final approximate concentration of 25 mM. For these particular precious metal salts, the *in situ* growth of the nanoparticles can be induced by the reduction of the salt to its metal form by the PVA itself with the PVA also acting as stabiliser (capping agent) for the nanoparticles and preventing agglomeration.[31]

Printed samples of Ag/PVA were prepared on acetone-cleaned glass substrates, heated to 40 °C during printing to assist with drying of the jetted fluid and to control the profile of the deposited droplets. After printing is completed a second heating stage is carried out, consisting of a modest thermal treatment to grow the nanoparticles (45 min. at 90 °C for Ag or 90 min at 110 °C for Au, ramped to these temperatures at a rate of 10 °C min^{-1}) and was performed simply on an open hot plate under ambient atmospheric conditions. The thermal processing conditions were selected on the basis of identifying the minimum temperature/time combinations required to maximise the extinction behaviour described in Section 3.5.

Fig. 2 shows detail of a printed line of the Ag/PVA nanocomposite (following the thermal treatment described above) and indicates the potential to form well-defined lines with good edge acuity. Printed droplet size is of the order of 50 μm in diameter so, with the programmed 50% droplet overlap, the depicted line is ~5 droplets wide. The yellow colouration of the line is a reasonably true representation of the actual observed colour that results from the SPR band of the Ag nanoparticles. In Fig. 2, it should be noted that the intensity of the colour is strongest in the centre of the line where the printed thickness is greatest, the line having a curved cross-sectional profile resulting from the coalescence of the droplets and contact line pinning of the edges – further optimisation of the droplet drying conditions are necessary to produce a flatter line profile. Typical line thicknesses, measured at their centre, were 200–250 nm for a single-pass printing process.

As the nanoparticles are formed within the PVA matrix only *after* the line structure has stabilised, their distribution will be uniform within the volume of the printed feature. Whilst drying effects will still affect the shape of the printed PVA droplets, moderate heating of the substrate (*i.e.* >40 °C) during printing rather than the more complex method of balancing a multi-solvent printing fluid medium can usually control the final feature profile. The nature of the line in Fig. 2 confirms that the nanoparticles have not been drawn to the edge of the printed feature when using the *in situ* formation of nanoparticles, thereby considerably reducing the impact of the classic "coffee stain" problem that afflicts nanoparticles that are free to move during the evaporative drying process of a printed fluid.

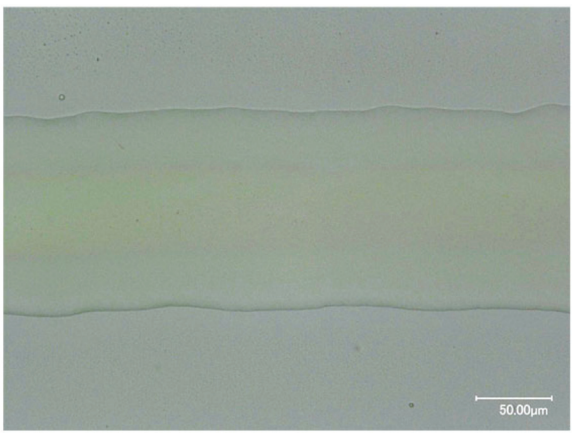

Fig. 2 Optical micrograph of a printed Ag/PVA feature following thermal treatment to generate Ag nanoparticles. The yellow tint to the printed feature arises from the surface plasmon resonance behaviour of the embedded Ag nanoparticles. Good edge quality is achieved using optimised printing conditions.

3.3 TEM analysis

Fig. 3 presents TEM images of the Ag/PVA and Au/PVA nanocomposite samples taken at low and intermediate magnifi-

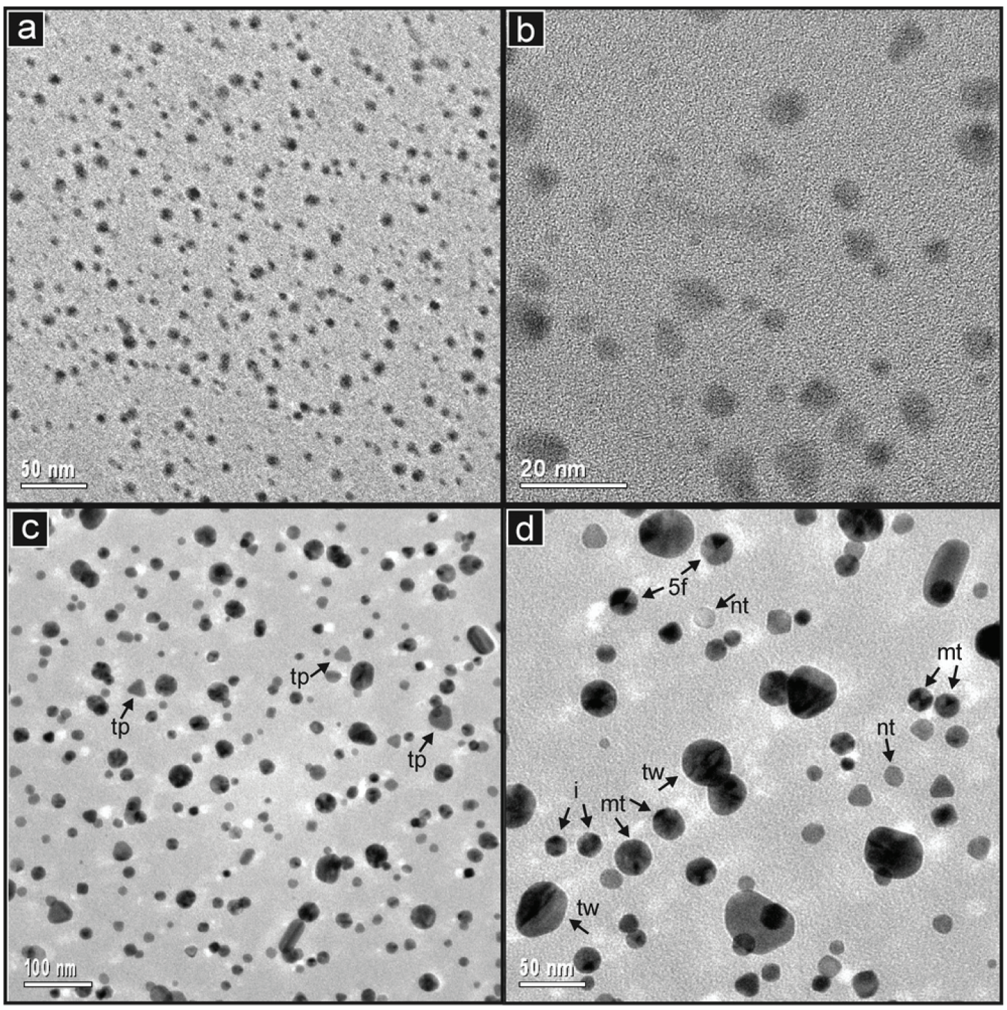

Fig. 3 Low and intermediate magnification TEM images of the (a, b) Ag/PVA and (c, d) Au/PVA samples. See text for meanings of labels in (c) and (d).

cations. Fig. 3(a) and (b) show the Ag particles to be uniformly distributed throughout the PVA medium and to fall into a narrow particle size range of between about 2 and 10 nm. Fig. 3 (b) clearly shows the amorphous polymer structure of the host PVA. The Ag particles appear to be roughly circular in profile but with considerable variation. No internal structure is visible in the nanoparticles at this magnification and there are no obvious highly symmetrical or twinned examples in these images.

Turning to the Au/PVA material, it is clear from the images in Fig. 3(c) and (d) that the particles are generally larger than those of Ag, at about 5–50 nm. The magnifications in Fig. 3(a) and (d) are the same. Many of the Au particles have high symmetry in profile and many show clear single and multiple twin boundaries. There is a wide range of particle morphologies. In Fig. 3(c) and (d) examples of twinned (labelled tw) and multiply-twinned (mt) particles as well as those with no visible twinning planes (nt) are identified. Particles which appear to be triangular plates (low contrast, so thin, with 3-fold symmetry in profile, labelled tp), particles with visible 5-fold twinning in profile (labelled 5f) and icosahedra (multiply twinned and with hexagonal profile, labelled i) are also indicated in Fig. 3(d). The particles with five-fold twinning may be either decahedra or icosahedra viewed along their C_5 axes. The triangular plates are expected to have twinning planes parallel to their large faces and therefore invisible when these are viewed in profile. Other particle geometries may include cubes, tetrahedra, octahedra and their truncated forms, beams, rods and bipyramids. An excellent review of nanoparticle morphologies has been published by Xia *et al.*[32] It is necessary to obtain high resolution images, as will be presented in Section 3.4, to determine particle morphology in most cases.

Lower magnification TEM images were analysed using the ImageJ software package[23,24] using a combination of its image processing and automated particle counting facilities to perform a quantitative particle size distribution analysis of the nanocomposite films. The distributions for the Ag/PVA and Au/PVA nanocomposite samples are presented in Fig. 4(a) and (b) using 1 nm and 2 nm data bins, respectively.

The distribution of Ag nanoparticles in Fig. 4(a) shows a remarkably well-defined Gaussian form (dotted black curve)

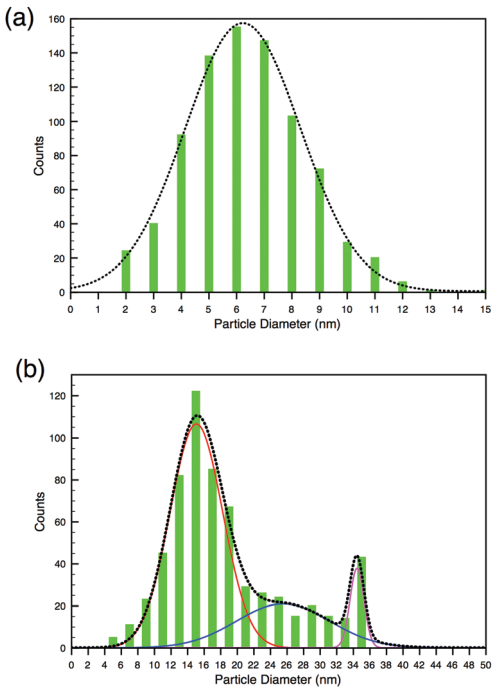

Fig. 4 Particle size distributions in (a) Ag/PVA nanocomposite showing simple Gaussian distribution of silver nanoparticles and (b) Au/PVA showing a more complex distribution reflecting the different families of Au nanoparticles formed within the PVA host matrix.

with a mean diameter of 6.5 nm. However, Fig. 4(b) shows a much more complicated form and wider size distribution in the Au/PVA sample, reflecting the broader range of Au particle sizes and structures shown in the TEM images of Fig. 3(c) and (d). The data representing this distribution was analysed using the peak deconvolution software package CasaXPS[33] which suggested the distribution could be modelled by considering three separate Gaussian distributions, centred at mean particle diameters of 15.1 nm (red curve), 25.5 nm (blue curve) and 34.4 nm (magenta curve). These sum to give the dotted black envelope in Fig. 4(b) which displays an excellent fitting to the overall distribution of the experimental data. Further examination of the TEM images indicates that the particles represented by the red distribution curve tend to have a very dark appearance, suggesting a small, 3-dimensional particle typified by the icosahedral and five-fold forms labelled i and 5f in Fig. 3 (d); whereas, the magenta Gaussian distribution (centred at 34.4 nm) tended to contain lower electron contrast (*i.e.* thinner) platelet-type particles. The third distribution, shown by the blue curve, is very broad and essentially covers the entire range of particle sizes. No distinct grouping of particle type could be associated with this distribution and it represents what can be considered to be a "background" of random particle shapes and sizes evolving within the PVA polymer matrix.

3.4 HRTEM analysis

Metallic Au and Ag both have face-centred cubic (fcc) structures of space group $Fm\bar{3}m$ (225) with lattice parameter, a = 4.078 Å (ref. 34) and a = 4.085 Å,[35] respectively. In the TEM, the most commonly observed diffraction spots are expected to be those corresponding to the (200) and (111) Miller planes which are both visible when these structures are viewed along the [011] zone axis. Within the expected accuracy of the TEM results, the respective interplanar spacings would be d_{200} = 2.04 Å and d_{111} = 2.35 Å for Au and d_{200} = 2.04 Å and d_{111} = 2.36 Å for Ag.

High resolution images of four individual Ag particles (circled) are presented in Fig. 5 along with corresponding DDPs and expanded images for each particle. The zone axes and the Miller indices are indicated in each DDP. The 5 nm diameter particle in Fig. 5(a) gives rise to a complete diffraction pattern consistent with the fcc structure of Ag as viewed along the [011] zone axis. The corresponding planes are clear in the expanded image. Since there are no unexpected spots in the DDP this particle is a single crystal. The particle in Fig. 5(b) again gives a complete DDP consistent with Ag viewed along the [011] direction. However, there are also unexpected spots in the DDP consistent with {111} planes but which are additional to the main pattern. Analysis of these by carrying out reverse Fourier transforms on only these additional spots showed that the corresponding planes are located at the bottom of the particle as viewed and that their orientations are indeed distorted away from the crystallographic orientation of the rest of the particle. This suggests they represent the start of crystal growth from planar defects near the edge of the particle by incorporation of new Ag, perhaps directed by the shape of the encapsulating polymer material. The particle in Fig. 5(c), in contrast, clearly contains a single twin boundary. The two crystal domains share a common set of {111} planes but each has its own set of {200} planes which are arranged at 28° to each other. Finally, the Ag particle in Fig. 5(d) contains three crystallographic orientations, despite its being only about 4 nm across. These are seen to give three pairs of spots in the DDP which are all consistent with {111} planes but are orientated at 120° to each other. The expanded image shows the particle to consist of three branches which appear to be joined at the particle centre. Reverse Fourier analysis on each of the three pairs of spots in turn showed that each corresponded to {111} planes in different branches, orientated as indicated by the arrows in the figure. This structure may capture the coalescence of the three smaller particles and may be a nucleus from which could grow a particle with three crystal domains, mutually rotated by 120°. The constrained conditions under which these particles form within the polymer matrix may cause a high incidence of polycrystalline particles.

Turning to HRTEM images of Au/PVA, in Fig. 6 an Au particle with three main crystal domains is observed. These domains are crystallographically inter-related as can be seen by examining the corresponding DDPs ((i) to (iv)). DDP (i) presents the pattern of fcc Au viewed along the [011] direction with extra intermediate spots caused by plane defects. These are indicated by arrows in the image in Fig. 6(b). The largest of the three crystal domains is triangular as viewed in Fig. 6(a) and gives rise to DDP (ii) which is consistent with Au viewed

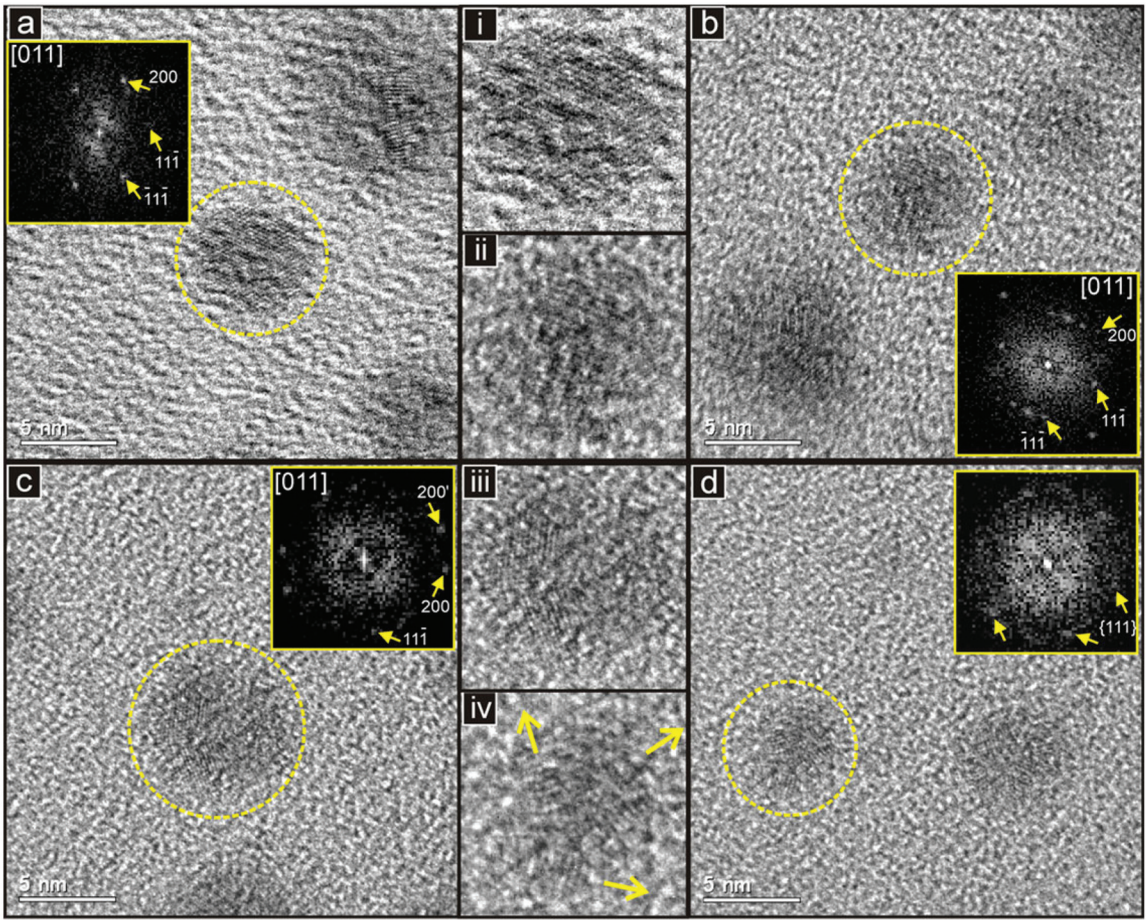

Fig. 5 TEM images of four individual Ag particles with accompanying DDPs inset. Magnified views of the images in (a)–(d) are given in (i)–(iv), respectively. See text for details.

down the [111] zone axis. This DDP contains additional unexpected spots, however. These are at 120° to each other and all represent lattice spacings of 2.50 Å. These are indexed as 1/3{422} reflections. These additional spots have been reported widely for Au nanoparticles and have been explained in three ways: (1) as the effect of twinning planes or stacking faults between (111) planes lying perpendicular to the electron beam; (2) to be caused by there being a number of (111) planes, n, perpendicular to the beam in a thin plate, where n is not divisible by 3 and so results in unequal numbers of A, B and C planes in the familiar ABC stacking arrangement; (3) that in such very small particles, the reciprocal lattice points are elongated allowing spots from the first Laue Zone to be visible in the [111] pattern. These explanations are discussed by Reyes-Gasga *et al.*[36] and in references therein. Determination of which explanation is valid in this work would require in-depth study of this particle and is beyond the scope of the current work. DDP (iii) contains a complete pattern corresponding to fcc Au as viewed along the [011] zone axis. DDP (iv) is taken from the whole of the image in Fig. 6(d) and shows that the (200) planes of domain (iii) are parallel with one set of 1/3(422) planes of domain (i). These planes are also parallel to the boundary between these two domains. A similar arrangement of planes exists in the image in Fig. 6(b). The parallel planes are clear in the image in both domains and are the (200) of domain (i) and one of the 1/3(422) planes of the central domain. From the DDPs it can be determined that the normal of the common planes in (b) is at 120° to the normal of the common planes in (d). This suggests that domains (i) and (iii) grew from domain (ii).

Fig. 7 shows a HRTEM image of a highly regular Au particle viewed down a C_5 axis of symmetry formed by five crystal domains which are separated by five visible twin planes. The Au crystal lattice is resolved throughout the particle and DDPs of each of the five domains (i) to (v) are presented in the figure. Each DDP contains a complete diffraction pattern of the cubic Au structure as viewed along the [011] zone axis. As is demonstrated by the rotation of the diffraction patterns in DDPs (i) to (v), the crystal structure of each domain is rotated by 72° with respect to those of the two domains neighbouring it. This occurs in such as way that the normal of the visible [200] planes of all five domains form radii of the particle. Such C_5 symmetry is consistent with two geometries common in Au nanoparticles, the icosahedron, which would have twin bound-

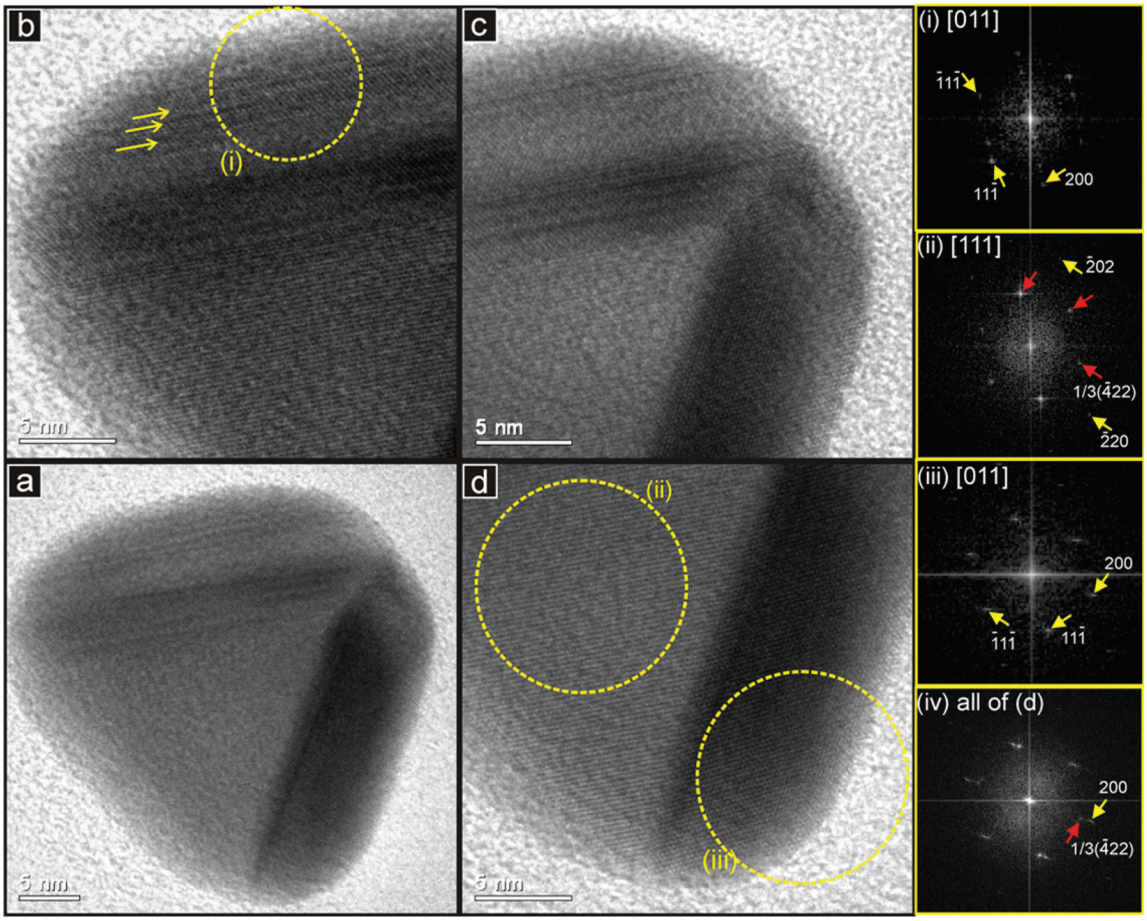

Fig. 6 TEM images of a doubly-twinned Au particle showing: (a) the whole particle and (b, c, d) the three corners. Circles indicate regions from which DDPs (i) to (iv) have been obtained. Zone axes and Miller indices of the spots are given in the DDPs. The arrows in (b) indicate a series of plane defects. See text for further details.

aries associated with all twenty edges and contain twenty tetrahedral crystal domains, and the decahedron, which would contain five tetrahedral domains which can be viewed as five interlocking "segments" sharing an edge along the C_5 axis of the particle. Since no twin boundaries additional to the five in C_5 symmetry are viewed in Fig. 7, and since the particle has an approximately circular profile – which would cause facets perpendicular to the beam to be convex – the particle is assigned to be a decahedron.

The images presented in Fig. 6–8 demonstrate that high resolution lattice images of the Ag and Au nanoparticles could be obtained, despite their being held within a relatively thick polymer matrix, and that DDPs could be generated from these to give detailed crystallographic information on particles down to 4 nm in diameter.

Undoubtedly, with such a disparity in size, shape and distribution between the Ag and Au nanoparticles, there is a fundamental difference between the mechanisms whereby the Ag and Au metal ions can come together to form nanoparticles within the PVA host material. In the case of gold, the $HAuCl_4$ precursor delivers the very unstable Au^{3+} ion, which is readily reduced by the PVA environment, likely to the Au^0 metallic form, thereby allowing movement over some distance through the PVA matrix due to its low level of interaction with the polymer, giving rise to the generation of larger, well-developed nanoparticles within the internal void structures of the PVA. The $AgNO_3$ precursor salt, on the other hand, delivers silver in the form of the much more stable Ag^+ ion, which will have a much longer lifetime within the PVA matrix. However, this greater stability will result in the Ag^+ ions interacting strongly with the PVA host, in particular with its associated –OH groups. This interaction will inhibit the mobility of the silver ions and decrease the distance over which they can diffuse to join together with each other to form nanoparticles. This may well explain why the seed-like Ag nanoparticles form in much larger number and are much smaller than the Au nanoparticles as imaged in Fig. 5.

3.5 Optical properties

If the printable nanocomposite materials are to be used in sensing or optical coupling applications, their absorption behaviour, driven by the presence of the nanoparticles, is of

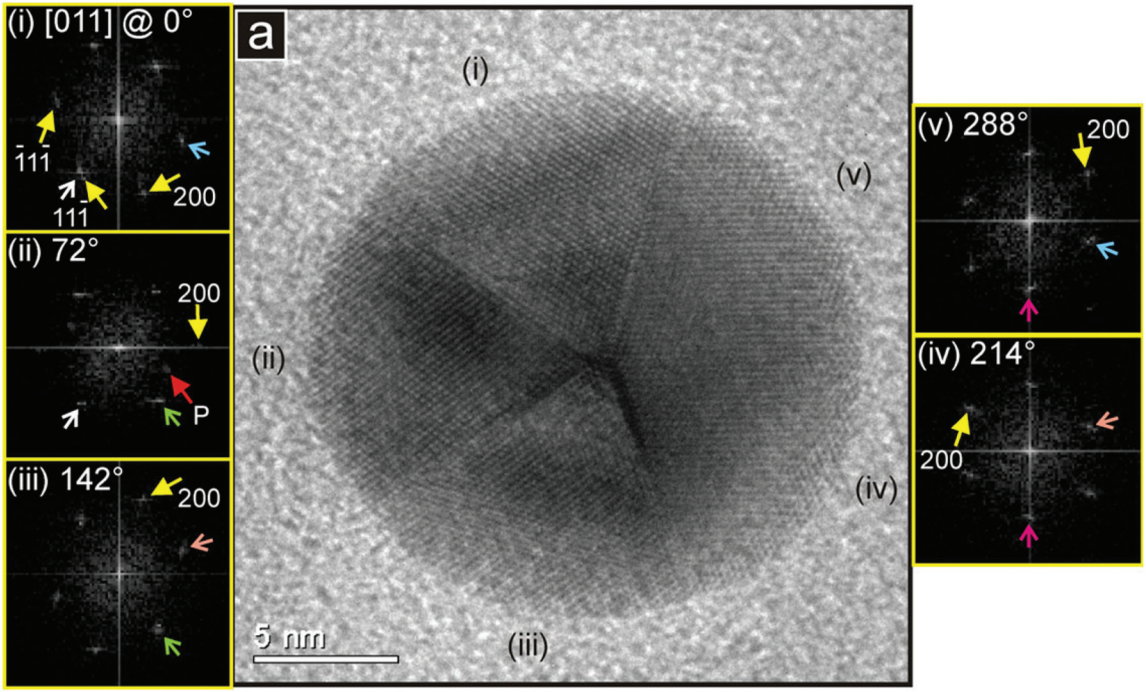

Fig. 7 (a) TEM image of a multiply-twinned Au particle showing five-fold symmetry viewed down its major (C_5) axis of symmetry. DDPs of each of the five visible crystal domains are presented as indicated on the image. These can all be indexed to the Au structure viewed along the [011] zone axis. All Miller planes are indicated in (i). In (ii)–(v) only the 200 planes are labelled. In the DDPs, the angles of rotation relating the patterns are given and small coloured arrows indicate {111} planes which are shared (*i.e.* continuous) between neighbouring domains. The extra spots marked P in (ii) are from an ordered region of the polymer near the edge of the particle.

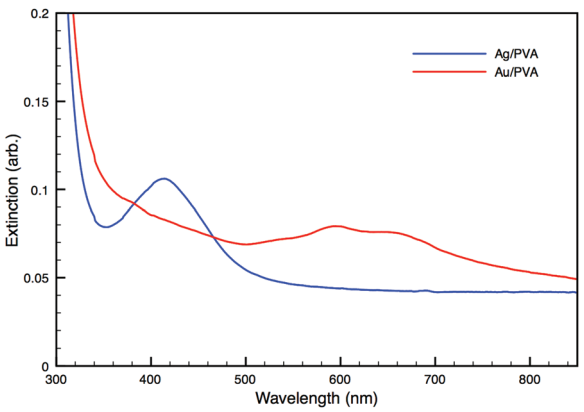

Fig. 8 Extinction spectra for the Ag/PVA and Au/PVA nanocomposite materials. The silver doped nanocomposite shows a well-defined peak at ~415 nm whereas the gold doped material shows a broader, multi-modal peak centred around ~620 nm.

fundamental interest. The optical extinction spectra taken of a deposited and thermally processed area of the printable fluids for both the Ag and Au nanocomposite materials are presented in Fig. 8. Here, from the spectrum depicted by the blue line, enhanced extinction can clearly be seen as a well-defined peak centred around 415 nm for the Ag-based composite material and this peak position is entirely consistent with the surface plasmon resonance behaviour reported for 5–6 nm diameter Ag nanoparticles dispersed in organic solvents.[37] Such a "clean" SPR response makes the Ag/PVA nanocomposite an excellent potential platform for SPR-based sensing elements and, indeed, has recently been employed[38] as a detector for ambient biogenic amines through suppression of the SPR response upon exposure to the air-borne amines. The Au/PVA nanocomposite extinction spectrum, shown as the red line in Fig. 8, is quite different from that for Ag/PVA, with a very broad and more structured absorption band extending between approximately 500–750 nm. A similar "peak" shape was reported by Kang and Wu[19] and was attributed to incomplete nanoparticle growth during their experiments on the photo-reduction of $HAuCl_4$ in PVA. In our case, the structure is most likely due to the variety of Au nanoparticle sizes and shapes that are able to form within the PVA host during the thermal processing stage. Whilst the absorption band shows some structure, it is not sufficient to perform unambiguous identification with specific Au nanoparticle forms. Based on previously published work[39,40] the region 500–750 nm is likely to result from a combination of SPR bands associated with small spherical, through dodecahedral/octahedral to elongated Au nanoparticles in order of increasing wavelength of the associated SPR peaks, along with a background absorption from other particle shapes such as the flat platelets. This range of nanoparticle shapes is clearly seen in the TEM images of Fig. 3(c) and (d). It is therefore not surprising to see a strong

correlation between the forms of the extinction spectra for these two nanocomposite materials and their respective particle size distribution envelopes as shown in Fig. 4 – *i.e.* sharply defined for the Ag/PVA material but much broader, and centred at longer wavelengths, for the Au/PVA.

The somewhat complex nature of the absorption characteristics of the Au/PVA nanocomposite will limit its use in optical applications owing to the reduced coupling and sensitivity to the incoming light and to its environment. This may ultimately be a limiting factor to the viability of this method of printing patterned areas of Au/PVA for device fabrication unless ways to restrict and tune the growth of the Au particles can be found.

4. Conclusions

We have been able to print, using commercially available inkjet technology representative of current manufacturing systems, PVA nanocomposites onto glass substrates. Critically, the nanoparticles in these composites are formed *in situ* after the printing process has defined the desired pattern, thereby retaining a uniform distribution of the nanoparticles within the patterned host PVA medium. This paves the way for a method of printing optical elements such as waveguides using these nanocomposite materials and the further addition of other optically active materials (*e.g.* dyes) to the PVA precursor can broaden the application in printed optical elements still further. The thermal processing of the nanocomposite films occurs at temperatures compatible with a wide range of substrate materials, including plastic films that could support roll-to-roll manufacturing processes. Importantly, the technique may be extended to other noble metals by changing the metal salt added to the PVA solution and has the potential to be used with other metallic systems if used in conjunction with a reductive "development" step replacing or supplementing the thermal processing stage post-printing.

HRTEM was used successfully to obtain high resolution lattice images of the Ag and Au nanoparticles despite these being suspended in a relatively thick polymer matrix. Diffraction patterns (DDPs) generated from these images provided detailed crystallographic information on the particles even at diameters down to around 4 nm and were especially useful in determining the geometric relationships between crystal domains in twinned and multiply-twinned nanoparticles.

Whilst the preparation method described here is easily able to deliver printable Ag/PVA-based nanocomposites containing well distributed nanoparticles, the polymer environment in which the nanoparticles grow does not yield monodisperse distributions of single-crystal entities in the case of gold. Clearly this is a considerable advantage for the silver-based material where the growth mechanisms produce essentially spherical, albeit polycrystalline, nanoparticles with a reasonably tight size range and well-defined SPR band. For this simple processing method, the gold nanoparticles that develop within the PVA polymer matrix take on a wide range of sizes, shapes and polycrystalline forms which are reflected in the broad extinction spectrum, greatly reducing the definition of the SPR band and its sensitivity to any change from external influences. This variation in size and shape of these Au nanoparticles is probably a result of their being allowed to grow inside cavities within the structure of the polymer host that are likely to exist in similarly wide ranges of size and shape.

In order to control this shape/size distribution of Au nanoparticles within the nanocomposite and generate a usefully distinct SPR behaviour, it is probably necessary to introduce some additional "guiding mechanism" to help govern the growth phase. Such mechanisms could conceivably be the use of additives in the PVA solution to homogenise the void structures in which the gold nanoparticles form, changing the metal precursor used to dope the PVA, or perhaps the use of external influences (*e.g.* illumination) to help drive preferential growth of the gold nanoparticles from their precursor "seed" structures. Undoubtedly the simplicity of the method described here comes with its limitations as a method for preparing optical devices and sensing elements based on Au nanoparticles. Nevertheless, it may form the basis for the development of methods capable of generating polymer composites containing sufficiently homogeneous nanoparticle populations. The characterisation methods developed in this work may enable future studies of the growth mechanisms of noble metal nanoparticles in polymer matrices and how these may be influenced by the preparation parameters.

Acknowledgements

This work was conducted under the aegis of the Engineering and Physical Sciences Research Council (EPSRC) of the United Kingdom (EP/I004173/1). Amin Abdolvand is an EPSRC Career Acceleration Fellow at the University of Dundee. TEM and HRTEM were performed at the Electron Microscopy Facility at the University of St Andrews. The authors are grateful to Dr Stephen Francis (University of St Andrews) for assistance with the peak deconvolution analysis. All data created during this research are openly available from the University of Dundee Institutional Repository at http://dx.doi.org/10.15132/10000102.

References

1 P. Calvert, *Chem. Mater.*, 2001, **13**, 3299.
2 S. B. Fuller, E. J. Wilhelm and J. M. Jacobson, *J. MEMS*, 2002, **11**, 54.
3 T. Aernouts, T. Aleksandrov, C. Girotto, J. Genoe and J. Poortmans, *Appl. Phys. Lett.*, 2008, **92**, 033306.
4 L. Gonzalez-Macia, A. Morrin, M. R. Smyth and A. J. Killard, *Analyst*, 2010, **135**, 845.
5 M. Singh, H. M. Haverinen, P. Dhagat and G. E. Jabbour, *Adv. Mater.*, 2010, **22**, 673.
6 R. D. Deegan, O. Bakajin, T. F. Dupont, G. Huber, S. R. Nagel and T. A. Witten, *Nature*, 1997, **389**, 827.

7 R. D. Deegan, O. Bakajin, T. F. Dupont, G. Huber, S. R. Nagel and T. A. Witten, *Phys. Rev. E: Stat. Phys., Plasmas, Fluids, Relat. Interdiscip. Top.*, 2000, **62**, 756.
8 H.-Y. Ko, J. Park, H. Shin and J. Moon, *Chem. Mater.*, 2004, **16**, 4212.
9 A. F. Routh and W. B. Zimmerman, *Chem. Eng. Sci.*, 2004, **59**, 2961.
10 J. Park and J. Moon, *Langmuir*, 2006, **22**, 3506.
11 D. Soltman and V. Subramanian, *Langmuir*, 2008, **24**, 2224.
12 G. Berteloot, A. Hoang, A. Daerr, H. P. Kavehpour, F. Lequeux and L. Limat, *J. Colloid Interface Sci.*, 2012, **370**, 155.
13 E. Tekin, P. J. Smith, S. Hoeppener, A. M. J. van den Berg, A. S. Susha, A. L. Rogach, J. Feldmann and U. S. Schubert, *Adv. Funct. Mater.*, 2007, **17**, 23.
14 H. Hu and R. G. Larson, *J. Phys. Chem. B*, 2006, **110**, 7090.
15 M. Majumder, C. S. Rendall, J. A. Eukel, J. Y. L. Wang, N. Behabtu, C. L. Pint, T.-Y. Liu, A. W. Orbaek, F. Mirri, J. Nam, A. R. Barron, R. H. Hauge, H. K. Schmidt and M. Pasquali, *J. Phys. Chem. B*, 2012, **116**, 6536.
16 S. Porel, S. Singh, S. S. Harsha, D. N. Rao and T. P. Radhakrishnan, *Chem. Mater.*, 2005, **17**, 9.
17 B. Karthikeyan, *Physica B*, 2005, **364**, 328.
18 S. Clémenson, D. Léonard, D. Sage, L. David and E. Espuche, *J. Polym. Sci., Part A: Polym. Chem.*, 2008, **46**, 2062.
19 B. Kang and J. W. Wu, *J. Korean Phys. Soc.*, 2006, **49**, 955.
20 R. Abargues, R. Gradess, J. Canet-Ferrer, K. Abderrafi, J. L. Valdes and J. M. Pastora, *New J. Chem.*, 2009, **33**, 913.
21 G. V. Ramesh, S. Porel and T. P. Radhakrishnan, *Chem. Soc. Rev.*, 2009, **38**, 2646.
22 R. Gradess, R. Abargues, A. Habbou, J. Canet-Ferrer, E. Pedrueza, A. Russell, J. L. Valdés and J. P. Martínez-Pastor, *J. Mater. Chem.*, 2009, **19**, 9233.
23 W. S. Rasband, *ImageJ*, U. S. National Institutes of Health, Bethesda, Maryland, USA, 1997–2015, http://imagej.nih.gov/ij/.
24 C. A. Schneider, W. S. Rasband and K. W. Eliceiri, *Nat. Methods*, 2012, **9**, 671.
25 R. Kumar, A. P. Singh, A. Kapoor and K. N. Tripathi, *Opt. Eng.*, 2004, **43**, 2134.
26 S. Porel, S. Singh and T. P. Radhakrishnan, *Chem. Commun.*, 2005, 2387.
27 X. Meng, K. Fujita, Y. Zong, S. Murai and K. Tanaka, *Appl. Phys. Lett.*, 2008, **92**, 201112.
28 F. L. Martin, *Vinyl Alcohol Polymers, Volume 8 - Kirk-Othmer Encyclopedia of Chemical Technology*, Wiley, 2002.
29 J.-C. Park, T. Ito, K.-O. Kim, K.-W. Kim, B.-S. Kim, M.-S. Khil, H.-Y. Kim and I.-S. Kim, *Polym. J.*, 2010, **42**, 273.
30 J.-S. Lee, K.-H. Choi, H.-D. Ghim, S.-S. Kim, D.-H. Chun, H.-Y. Kim and W.-S. Lyoo, *J. Appl. Polym. Sci.*, 2004, **93**, 1638.
31 L. Longenberger and G. Mills, *J. Phys. Chem.*, 1995, **99**, 475.
32 Y. Xia, Y. Xiong, B. Lim and S. E. Skrabalak, *Angew. Chem., Int. Ed.*, 2009, **48**, 60.
33 *CasaXPS processing software for spectral and imaging data*, Casa Software Limited, http://www.casaxps.com, site accessed on 30/03/2015.
34 A. Maeland and T. B. Flanagan, *Can. J. Phys.*, 1964, **42**, 2364.
35 L.-g. Liu and W. A. Bassett, *J. Appl. Phys.*, 1973, **44**, 1475.
36 J. Reyes-Gasga, A. Gómez-Rodríguez, X. Gao and M. José-Yacamán, *Ultramicroscopy*, 2008, **108**, 929.
37 S. Peng, J. M. McMahon, G. C. Schatz, S. K. Gray and Y. Sun, *Proc. Natl. Acad. Sci. U. S. A.*, 2010, **107**, 14530.
38 R. Abargues, P. J. Rodriguez-Canto, S. Albert, I. Suarez and J. P. Martínez-Pastor, *J. Mater. Chem. C*, 2014, **2**, 908.
39 P. K. Jain, K. S. Lee, I. H. El-Sayed and M. A. El-Sayed, *J. Phys. Chem. B*, 2006, **110**, 7238.
40 A. A. Ashkarran and A. Bayat, *Int. Nano Lett.*, 2013, **3**, 50.